

LARGE EDDY SIMULATION OF HEAT TRANSFER WITHIN A MULTI-PERFORATION SYNTHETIC JETS CONFIGURATION

Soizic Esnault*, Florent Duchaine, Laurent Gicquel
CFD Team CERFACS
Toulouse, France
soizic.esnault@cerfacs.fr

Stéphane Moreau
Sherbrooke University
Canada

ABSTRACT

Synthetic jets are produced by devices that enable a suction phase followed by an ejection phase. The resulting mean mass budget is hence null and no addition of mass in the system is required. These particular jets have especially been considered for some years for flow control applications. They also display features that can become of interest to enhance heat exchanges, for example for wall cooling issues. Synthetic jets can be generated through different mechanisms, such as acoustics by making use of a Helmholtz resonator or through the motion of a piston as in an experience mounted at Institut Pprime in France. The objective of this specific experiment is to understand how synthetic jets can enhance heat transfer in a multi-perforated configuration. As a complement to this experimental set up, Large-Eddy Simulations are produced and analysed in the present document to investigate the flow behavior as well as the impact of the synthetic jets on wall heat transfer.

The experimental system considered here consists in a perforated heated plate, each perforation being above a cavity where a piston is used to control the synthetic jets. Placed in a wind tunnel test section, the device can be studied with a grazing flow and multiple operating points are available. The one considered here implies a grazing flow velocity of 12.8 m.s^{-1} , corresponding to a Mach number around 0.04, and a piston displacement of 22 mm peak-to-peak at a frequency of 12.8 Hz. These two latter parameters lead to a jet Reynolds number of about 830.

A good agreement is found between numerical results and experimental data. The simulations are then used to provide a detailed understanding of the flow. Two main behaviours are found, depending on the considered mid-period. During the ejection phase, the flow transitions to turbulence and the formation of characteristic structures is

*Address all correspondence to this author.

observed; the plate is efficiently cooled. During the suction phase the main flow is stabilised; the heat enhancement is particularly efficient in the hole wakes but not between them, leading to a heterogeneous temperature field.

INTRODUCTION

Synthetic jets can be induced by a moving device, such as a piston or a piezoelectric membrane at the bottom of a cavity. An acoustic excitation can also be used as employed by a Helmholtz resonator. These specific jets are characterized by the succession of suction and ejection phases, leading to a null mean mass budget. This particular behaviour has been proven very useful for flow control [1] or electronic cooling [2, 3], and is naturally present in acoustic liners of fan ducts [4].

The formation and the aerodynamic characteristics of synthetic jets have been studied for a few decades. Holman *et al.* [5] investigated synthetic jets and gave a formation criterion: the inverse of the jet Strouhal number should not be lower than a threshold depending on geometric parameters. Below this threshold, the flow emitted during this ejection phase is entirely sucked back within the cavity during the aspiration phase, thus no jet is formed. Smith and Swift [6, 7] experimentally studied the flow behaviour in the presence of synthetic jets and compared it to continuous jets. They showed that, while synthetic and continuous jets are quite similar in the far field, they present different behaviours in the near field, due to the vortex pairs created at the ejection phase. Synthetic jets are wider and slower than continuous jets. Leschziner and Lardeau [8] delivered a review of the state-of-the-art in numerical simulation of synthetic jets, targeting flow control applications. They distinguished slot jets from round jets, and detailed the flow behaviour in these cross-flow configurations. Lardeau and Leschziner [9] also focused on round synthetic jet interactions with a turbulent boundary layer, considering the separation from a rounded ramp. Such configurations of synthetic jets were facing a crossflow. Their behaviour could thus be compared to that of classic continuous jets in cross-flow [10, 11].

The synthetic jets impact on the boundary layer flow was studied targeting flow control applications. Amitay and Glezer [1] experimentally considered the aerodynamic performance of an unconventional airfoil, while controlling the flow by use of synthetic jets. Nae [12] performed numerical simulations of the unsteady flow control around the NACA 0012 airfoil and a circular cylinder with synthetic jet actuators. Wen and Tang [13] investigated the hairpin vortices formed by the jets, in laminar and turbulent cross-flow boundary layer configurations. Helmholtz resonators have also been investigated as a passive system to trigger synthetic jets necessary for the flow control. Yang and Spedding [14] considered this specific aspect experimentally and Bodart *et al.* [15] numerically. Targeting a different application, Zhang and Bodony [16] numerically studied the impact of different grazing boundary layers on the performance of honeycomb acoustic liners.

Jets are also widely used to deal with heat transfer enhancement issues [17]. In this domain, continuous or pulsed impinging jets have been studied. Synthetic jets also present specific features that could be useful in such cases. An advantage over continuous or pulsed jets is their zero-net-mass-flux character: no additional duct is required to add flow

within the system. Persoons *et al.* [18] proposed a review of impinging jets, focusing on the interests of synthetic jets. Regarding impinging synthetic jets, they proposed a correlation for the stagnation point heat transfer performance, depending on the Reynolds number, the jet-to-surface spacing and the stroke length. Following this study, McGuinn *et al.* [19] investigated more precisely the flow behaviour of an impinging, axisymmetric synthetic jet, treating wide ranges of jet-to-surface spacing and stroke lengths. They identified four "free synthetic jet flow morphology" regimes, depending on the stroke length, and four "impinging synthetic jet flow" regimes depending on the ratio of the stroke length to the nozzle-to-surface spacing. Trávníček and Tesař [3] considered an annular synthetic jet in an impinging configuration and evidenced different flow behaviours, depending on the driving amplitude level and frequency. Arik *et al.* [2] found out that, in some impinging configurations, synthetic jets present a higher cooling performance than steady jets, attributed to vortex shedding.

Considering turbomachinery applications, synthetic jets present some interesting features for the nacelle heat enhancement. Modern civil aircraft engines undergo an increasing core temperature and cooling needs to be more and more efficient. To do so, it could be of interest to use the synthetic jets formed thanks to the acoustic liners already present within the fan channel. These liners usually consist of Helmholtz resonator nets where the synthetic jet phenomenon is used to damp the noise coming from the fan. The configuration differs from an impinging configuration: the wall that would be cooled down by the jets is the perforated plate supporting the jet actuators, while the jets are facing a grazing flow. Duchaine [4] performed a sensitivity analysis of the heat transfer within such a configuration with Large Eddy Simulations (LES). This CFD method is adequate to consider such an unsteady and transitional physical process, compared to other methods: RANS is indeed not adequate, while DNS would be too expensive [8]. To the authors' knowledge, this work is among the first studying heat enhancement within acoustic liners. Both experimental and numerical research on synthetic jets is usually more focused on isolated, impinging jets. Manning *et al.* [20] considered synthetic jets cooling the plate they are coming from, in a single- and a four-orifice configurations, without the presence of a grazing flow. Giachetti *et al.* proposed to use synthetic jets for heat enhancement in a crossflow configuration [21]. Then, they extended it to a multi-perforation configuration [22] that can be seen as a geometric similitude of an acoustic liner in low Mach conditions, where synthetic jets are not induced by Helmholtz's resonators but through the motion of pistons. A parametric study on the pistons and main flow velocities was performed. Comparing their results to the theoretical case of a flat plate without perforation and with a case with steady pistons (*i. e.* no synthetic jets) they evidenced the significant impact of the synthetic jets on the wall heat transfer. This effect increases with the jet velocity on cross-flow velocity ratio. Through LES, the present study aims at reproducing the multi-perforation configuration they proposed, in order to better understand how the main flow structures impact heat transfer at wall.

In this paper, after describing the configuration and the numerical models, simulations with two meshes (a coarse and a finer automatically adapted) are used to describe the flow behaviour and give an overview of the main flow structures.

They are then compared to the experimental data, and a detailed understanding of the flow is provided, with the study of the boundary layer development. The aerodynamic impact on the wall temperature and convective heat transfer coefficient is finally investigated.

EXPERIMENTAL TEST CASE

The experimental set-up consists in a perforated plate, placed within the test section of a wind tunnel (Fig. 1). The 50 holes, whose common diameter is $D = 6.25$ mm, are distributed in 5 lines of 10 rows. The lateral and spanwise hole distances equal $2.8D$. Under each perforation, a dedicated cavity leads to a piston. A description of the plaque and cavity dimensions is given in Fig. 2. The 50 corresponding pistons are activated by the same engine and thus follow a similar movement, that leads to the formation of synchronised synthetic jets. For the present study, this movement is assumed to be perfectly sinusoidal:

$$Z_{pistons}(t) = Z_{mean} + K \sin(2\pi ft), \quad (1)$$

where Z_{mean} is the mean vertical position of the pistons, and K and f are the amplitude and frequency of the pistons, respectively. The piston positions and velocities over one period of their motion are shown in a phase diagram in Fig. 3, for $Z_{mean} = 0$ mm. Note that the instants described in this figure ($t = 0$, $t = T/4$, $T = T/2$ and $T = 3T/4$) are the ones used later on in this paper to describe the flow physics. A more detailed description of the experimental set-up is given in [22], along with the measurement techniques for aerodynamic and heat transfer.

In the experimental configuration, several operating points are available with different piston velocities and frequencies, as well as different injected velocities at the inlet. Since the average velocity of a synthetic jet is null, the resulting flow needs to be characterized by specific, dedicated parameters. For this study, we use the mean ejection velocity as used by Giachetti *et al.* [22] and as initially proposed by Holman *et al.* [5]. The jet velocity w is averaged over the ejection mid-period $\frac{T}{2} = \frac{1}{2f}$ at the jet exit surface, A :

$$\bar{W} = 2f \frac{1}{A} \int_A \int_0^{1/2f} w(t, x) dt dA. \quad (2)$$

With this definition of \bar{W} and the hole diameter D , three parameters characterizing the synthetic jets can be considered: the

Reynolds number Re , the Strouhal number St and the dimensionless stroke length $\frac{L_0}{D}$. They are defined as follows:

$$Re = \frac{\bar{W}D}{\nu}, St = \frac{2\pi fD}{\bar{W}}, \frac{L_0}{D} = \frac{\bar{W}}{2fD}. \quad (3)$$

This study focuses on one specific operating point: $K = 11$ mm and $f = 12.8$ Hz, which corresponds to an average velocity along the ejection mid-period of $\bar{W} = 2.07$ m.s⁻¹, leading to $Re = 830$, $St = 0.24$ and $\frac{L_0}{D} = 12.9$. The freestream velocity within the wind tunnel is $U_0 = 12.8$ m.s⁻¹, corresponding to a Mach number around 0.04 and a velocity ratio $\bar{W}/U_0 = 0.16$. The velocity profile at the inlet is turbulent, with turbulent intensity equal to 10.5 % in the experimental data. The plate is heated to study wall heat transfer. A regression method is used by Giachetti *et. al.* [21, 22] to determine the convective heat transfer coefficient h . It consists in imposing several heat fluxes while measuring the plate temperature; h is then fitted using Newton's cooling law $\phi = h(T_w - T_{ref})$.

Finally, the available experimental data consists in the time averaged velocity within the symmetry plane of the configuration, on top of the perforations, and the average convective heat transfer coefficient h field along the perforated plate.

LARGE EDDY SIMULATIONS MODELING

The simulations rely on the use of the AVBP solver, co-developed by Cerfacs and IFPEN. This code solves the compressible Navier-Stokes equations. For the present work, the Lax-Wendroff (LW) numerical scheme [23], 2nd order in time and space, is used. Predictions are obtained thanks to two different sub-grid-scale models: a classic Smagorinsky model [24] is used for the first simulation before switching to the σ model [25]. Only the second model reproduces the correct behaviour of turbulent viscosity close to walls, mandatory for wall resolved simulations as targeted in this study.

The numerical domain considered for the simulations represents a section of the wind tunnel test section: the upstream part of the test section is not considered and the inlet of the domain corresponds to the location where velocity starts to be measured. The other boundaries of the domain correspond to the actual transverse and longitudinal dimensions of the experimental set-up. The frame origin is located at the inlet (the beginning of the perforated plate) for the axial direction, on the symmetry plane for the transverse direction and at the perforated plate for the vertical direction.

The inlet and the outlet boundary conditions of the numerical domain are treated with the NSCBC (Navier-Stokes Characteristic Boundary Conditions) formalism [26]. A velocity profile is imposed at the inlet, provided from experimental data (Fig. 4). A difference that needs to be noticed is the absence of turbulence injected at inlet in the numerical set-up: it was chosen to neglect its impact in this initial work. Future work will be devoted to specifically address this point. A constant pressure $P_0 = 101325$ Pa is imposed at the outlet, which is treated with the three-dimensional extension of the traditional

LODI (Local One Dimensional Inviscid formulation) method [26] developed by Granet *et al.* [27], using space-averaged values. The side walls and the ceiling of the test section are treated as slip walls. They are far enough from the zone of interest, *i. e.* the plate and cavities, to not interact with the flow at this investigated location. The bottom wall, the perforated plate and the cavities are non slip walls. To determine the heat transfer coefficient h , two heat fluxes are considered on the perforated plate: 1500 W.m^{-2} and 500 W.m^{-2} .

To reproduce numerically the movement of the pistons, a moving mesh methodology is considered. It uses the ALE (Arbitrary Lagrangian-Eulerian) formalism [28]. The mesh is divided into two parts: the static part, corresponding to the test section and the upper parts of the cavities, and the moving part, corresponding to the pistons and the lower part of the cavities. In this latter part, during a cycle, mesh cells are compressed and stretched and velocity is imposed on the piston walls. The initial position of the mesh is the medium course of the pistons.

Two fully tetrahedral meshes are used for the study. The first one, M1, contains only 13 million elements and is used to initialise the simulations. The second one, M2, contains 66 million elements. Mesh M1 is user-designed. Some refining effort is made around the plate and cavities, but it is quite coarse. On the contrary, mesh M2 comes from an automatic adaptation method. The goal is to enhance the mesh within the areas where there is either an important velocity gradient or an important value of normalized wall distance Y^+ . The mesh adaptation strategy is inspired from [29]. A first simulation with the coarse mesh M1 provides fields averaged over six periods of the pistons motion to define a metric that is then used to adapt the mesh. This metric is a field based on physical quantities that can take any positive values. Wherever it is greater than 1, the mesh will be coarsened; on the contrary, when it is lower than 1, it is refined. The farther the value is from 1, the more important is the refinement or coarsening. In this study, only refinement is targeted leading to $metric < 1$. It is chosen to fix the maximum value of the metric to $\epsilon_{max} = 0.9$. Likewise, a minimal threshold $\epsilon_{min} = 0.3$ is defined to avoid too small cells. Since the adaptation does not require to be very important far from the perforated plate, the metric is first put to ϵ_{max} in the whole domain, and a zone of interest is defined around the perforated plate. Within this zone, results from a simulation with M1 are used to compute the metric.

The metric used is based on a double criterion: velocity gradients and Y^+ at wall. The aim is to refine the mesh within the boundary layer, especially where it is impacted by the synthetic jets. It is defined from the non-dimensional number Φ :

at walls, if $Y^+ > Y^+_{target}$.

$$\Phi = Y^+_{target} / Y^+ \quad (4)$$

within the flow:

$$\Phi = \left[1 - \frac{|\overline{\nabla}(\|\vec{U}\|)| - |\overline{\nabla}(\|\vec{U}\|)|_{min}}{|\overline{\nabla}(\|\vec{U}\|)|_{max} - |\overline{\nabla}(\|\vec{U}\|)|_{min}} \right]^\alpha \quad (5)$$

In the first case, $Y_{target}^+ = 1$ since we are targeting wall resolved simulations. In the second case, the normalized velocity gradient, $|\overline{\nabla}(\|\vec{U}\|)|$, is defined as:

$$|\overline{\nabla}(\|\vec{U}\|)| = \|\overline{\text{grad}}(\sqrt{u^2 + v^2 + w^2})\|, \quad (6)$$

where $\overline{}$ stands for a time average operation, $|\overline{\nabla}(\|\vec{U}\|)|_{min}$ and $|\overline{\nabla}(\|\vec{U}\|)|_{max}$ are the minimal and maximal values of the $|\overline{\nabla}(\|\vec{U}\|)|$ field, respectively; α is used to control the cell dilatation within the mesh [29], a low value will generate less cells while a too high value will increase too much their number within the domain. Here it is equal to 50. Finally, with the two thresholds previously described, $\varepsilon_{min} = 0.3$ and $\varepsilon_{max} = 0.9$, the metric used for grid adaptation is given by:

$$metric = \Phi(\varepsilon_{max} - \varepsilon_{min}) + \varepsilon_{min}. \quad (7)$$

For comparison, a cut on the symmetry plane of meshes M1 and M2, focusing on the perforated plate zone (the whole cavities and the entire test section are not shown), is given on Fig. 5. The adaptation leads to a mesh adequately refined at wall along the perforated plate, as is confirmed by the Y^+ fields (Fig. 6). For the average field, the mean Y^+ is equal to 3.7 for M2. The mean Y^+ is equal to 3.7 and 3.6 at $t = T/4$ and $t = 3T/4$, respectively. Moreover, there are approximately 40 cells in the diameter of a hole for M2 and, considering a 5 mm-high neck, the mean Y^+ for the average field is equal to 3.4.

GENERAL DESCRIPTION OF THE FLOW

Figure 7 provides instantaneous views of the axial velocity in the symmetry plane and the wall shear stress along the perforated plate for the simulation using M2. Four instants are provided, corresponding to the four specific points evidenced on Fig. 3. For every moment, the shear stress decreases from the inlet to the first row of holes due to an increase of the boundary layer thickness. Then, the pistons motion induces two different phases: the ejection (Figs. 7a and 7b) and the suction (Figs. 7c and 7d) mid-periods. The flow behaviour in the perforation region is significantly different between

these two mid-periods. During the ejection phase, the jets interact with the incoming boundary layer leading to the creation of unstable shear layers. The boundary layer is thus destabilised with the formation of different coherent structures and turbulence increases. These structures are then convected by the flow, as seen on Fig. 7a and 7b on the symmetry plane. Their impact on the plate can be noticed through their footprint on the wall shear stress. In particular, horseshoe vortices are clearly identifiable around the first row of holes, at $t = 0$ (Fig. 7a). On the contrary, during the suction mid-period, the boundary layer is sucked by the jets stabilising it. Between the holes, one can observe the development of an undisturbed boundary layer until the end of the plate. Within the hole wakes, the boundary layer is clearly seen to be sucked by each perforation. A new boundary layer then starts to develop after each hole, leading to a local increase of the shear stress. These phenomena are visible at $t = T/2$ and even more clearly at $t = 3T/4$, respectively in Figs. 7c and 7d.

Looking at coherent structures thanks to the Q criterion (Fig. 8), horseshoe vortices can be seen along the first row of cavities at $t = 0$ (A in Fig. 8a). Their presence is due to a blockage effect, linked to the presence of the jets: the incoming grazing flow gets blocked by the jets, and thus circumvents them. Some structures that seem to be counter rotating vortex pairs are visible (B in Fig. 8a). These structures are characteristic of jets in cross-flow [10, 11]. Downstream the jets, several rows of bigger structures can be spotted on top of the others (C in Fig. 8a), corresponding to vortices generated around the first rows of jets before $t = 0$ and then convected. We identify these as shear layer vortices. These structures are mainly created by the unstable shear layer at the jet interface with the main grazing flow. They are also similar to hairpin vortices, such as the structures showed by Wen and Tang [13], on a different operating point. Downstream, the flow seems more turbulent and mixed. Only smaller, mixed structures can be spotted. This turbulent zone is the result of the destabilisation and interaction between the upstream structures and the jets. The first rows of jets is the first to be impacted by the incoming boundary layer: the following jets are impacted by a flow that is already more turbulent. All these different structures are convected by the main flow, as can be seen through the comparison of the Q criterion at $t = 0$ (Fig. 8a) and $t = T/4$ (Fig. 8b). It can also be noticed that the structures are at first concentrated within the hole wakes, the space between the perforations being free of any structures, at least until the third row of holes (Fig. 8a). Then, at the end of the ejection period (Fig. 8b), the mixing of the flow has been enhanced by all the structures that are not any more aligned in the axial direction and spread laterally on the whole plate.

As seen on Fig. 9, the flow behaviour is not as detailed with M1 than with M2. Indeed, M2 is more refined within the boundary layer, targeting a wall resolved simulation. Moreover, the σ model is used for the simulation with M2, in place of the Smagorinsky model with M1, leading to better flow predictions near the wall. Velocity gradients are sharper with M2 and the axial velocity field contains more flow structures with M2 than with M1. During the ejection mid-period, some of these structures impact the plate temperature T_w fields that show significant differences from one mesh to the next.

COMPARISON WITH EXPERIMENTAL DATA

Velocity fields are compared to the available experimental data on the symmetry plane of the domain in Fig. 10. To do so, only time averaged fields are considered, the numerical results being averaged over five periods of the pistons motion. Convergence has been checked by comparing 3- and 4- to 5-period averaging. The experimental uncertainty is estimated at 4% for the mean velocities, and at 8% for the root mean square (*rms*) values [22]. Figures 10a to 10d present the mean axial, mean vertical, *rms* axial and *rms* vertical fields, respectively. The corresponding dimensionless velocity profiles are shown on Fig. 10e to 10h. The six profiles are taken at the following positions: the beginning of the plate ($x/D = 0$), the center of the first row of holes ($x/D = 8$), the center of the fourth row of holes ($x/D = 16.4$), the center of the seventh row of holes ($x/D = 28.4$), the center of the tenth (and last) row of holes ($x/D = 33.2$) and finally downstream the perforated plate ($x/D = 40$). Note that the x/X_0 part of the dimensionless velocity profiles is just a way to artificially shift the profiles, for the sake of clarity. X_0 is equal to 0.1 for axial mean and *rms* profiles, and 0.05 for the vertical mean and *rms* profiles.

The averaged velocity fields show that the boundary layer thickens faster than a boundary layer on a flat plate. Some fluctuations can be seen as early as since the first row of holes, leading to a progressive thickening of the boundary layer. This behaviour of the boundary layer is also visible with the velocity profiles. These velocity fields also show that the simulation with M1 reproduces the good orders of magnitude, especially far from the plate, but tends to overestimate the boundary layer displacement, as well as the jet penetration heights within the main flow. The simulation with M2 produces much better results if compared to the experimental data. This is confirmed by the velocity profiles: M1 overestimates velocities within the boundary layer, while M2 reproduces the flow behaviour quite well. Vertical velocity profiles are not as well predicted as the axial velocity profiles. A second level of refinement or a higher order numerical scheme would probably help to better capture the profiles. Nonetheless this is out of the scope of the present study for which the results are satisfactory.

Looking at *rms* fields and profiles, some differences are observed between the experimental data and the numerical results. It should be reminded that no turbulence is injected at the inlet of the simulations, which is different from the experimental case. The measurement techniques can also explain some of the observed differences. Indeed, fluctuations are observed for the left part of the experimental data that come to a certain extent from the lack of seeding particles far from the plate. Differences between the experimental data and the numerical results very close to the plate can also partly be explained by the measurement technique, that is also restricted when too close to walls.

Despite known limitations from the experience and the simulations, these comparisons enable us to be quite confident about the results given by the simulation on M2. In particular, the flow behaviour within the boundary layer is well reproduced. Using this simulation, the next section investigates the flow development in the presence of the synthetic jets.

ANALYSIS OF THE FLOW DEVELOPMENT

To better understand the impact of synthetic jets on wall heat transfer, the flow development on the plate is analysed more deeply hereafter. In particular, the development of the boundary layer is considered. The axial velocity profiles are compared at different instants and positions and the flow footprint on the plate is observed through the wall shear stress. Finally, the plate temperature is considered at different instants and confronted to these elements, and the mean convective heat transfer coefficient is printed against experimental results. Note that all this part of the study is made using only simulations obtained with M2.

Boundary layer development

As pointed out previously, an undisturbed boundary layer develops from the inlet to the first row of holes, while the flow around the perforations presents two distinct behaviours which depend on the considered mid-period. Figure 11 compares these evolutions, at $t = T/4$ and $T = 3T/4$, by looking at the axial velocity profiles at different positions along the plate. The profiles are taken at the same axial positions as for the comparisons of averaged fields, in Fig. 10. Figure 11 also compares the wall shear stress over two different lines (the symmetry line and inbetween the holes) on the plate that are described in Fig. 2 and correspond to the same instants. Note that the grey dashed vertical lines correspond to the limits of the holes where the wall shear stress cannot be computed.

During the ejection mid-period, the jets induce the presence of unstable shear layers that lead to the creation of vortices such as the structures previously described and turbulence generation. The velocity profiles at $t = T/4$ (Fig. 11a) show some perturbations illustrating the chaotic behaviour of the flow. Meanwhile, the wall shear stress presents important fluctuations all along the plate (Fig. 11c), due to the flow structures. Looking back to the wall shear stress field along the plate in Fig. 7, it can be seen that the whole perforated area of the plate is impacted. The wall shear stress appears to be quite higher inbetween the holes than in the hole wakes, implying that the structures impact on the plate is higher in the hole periphery than in their wake. This is coherent with the mixing enhancement that was observed when considering the Q criterion.

The boundary layer remains undisturbed on the entire plate during an important part of the suction phase, as can be seen on the axial velocity profiles at $t = 3T/4$ on Fig. 11b. Indeed, the profiles inbetween the hole lines are characteristic of the development of a boundary layer on a flat plate: its thickening lead to a decrease of the wall shear stress. Within the hole wakes, the profiles are different: the flow is sucked within the cavities and the boundary layer restarts at the end of each perforation. The wall shear stress globally increases but, despite the important fluctuations, a small decreasing tendency can be spotted between two following holes, in accordance with the idea that the boundary layer restarts after a hole. Finally, after the ten rows of perforations, the wall shear stress within the hole wakes starts decreasing again, corresponding to a

developing boundary layer.

Resulting plate wall temperatures and heat transfer

In the previous section, different flow parameters were studied to better understand the development of the boundary layer and the impact of the synthetic jets on the perforated plate. It can now be used to consider the wall heat transfer. Figure 12 gives the wall temperature along the plate at the different instants previously described, for a 1500 W.m^{-2} wall heat flux. Two elements, coherent with the previous results, can first be pointed out:

- the temperature field from the inlet to the first row of holes corresponds to a developing thermal boundary layer;
- the ejection and suction phases present distinct behaviours.

During the ejection mid-period, the impact of the different structures that have been identified can be observed in the temperature field. The blockage effect is visible at $t = 0$ (Fig. 12a): the horse-shoe vortices can be detected around the first line of holes and the circumvention of the jets appears clearly in the temperature field. The vortices bring the cold incoming flow nearer to the hot plate, leading to a higher thermal gradient and a thinner thermal boundary layer. The alignment of the structures, followed by their mixing along the plate during the ejection mid-phase and the increase of turbulence, that have been noticed with the study of the Q criterion (Fig. 8) is also retrieved here, when comparing the temperature fields at $t = 0$ (Fig. 12a) and $t = T/4$ (Fig. 12b). Comparing the wall temperature field within the perforated area of the plate with unperforated regions on the lateral sides, it can be stated that the vortices generated during the ejection mid-period contribute to efficiently cool down the plate. The temperature within the perforated area is indeed lower at the end of the mid-period compared to the side regions.

In a similar way, the temperature evolution during the suction period can be understood through the previous observations of the boundary layer development. The hole wakes present a significantly lower wall temperature than the rest of the plate; the space between the holes presents a rising temperature once the impact of the vortices has been convected by the main flow. Coming back to the axial velocity profiles at $t = 3T/4$ (Fig. 11b) and corresponding wall shear stress (Fig. 11d), the boundary layer development explains the phenomenon. Within the hole wakes, the flow gets sucked by the jets within the holes and the boundary layer becomes thinner, starting again at the end of each hole. The wall shear stress increases. This contributes to a thin thermal boundary layer within the hole wakes, and thus colder temperatures. On the contrary, between the hole lines, the flow is not disturbed by the jets, leading to a developing boundary layer. The thermal boundary layer develops in a similar way, thickening along the plate and leading to higher wall temperatures.

The plate temperature field averaged over five periods of the piston motion is given in Fig. 13. The developing boundary layer at the inlet is retrieved. The effects of both mid-periods can be noticed, in a smoother way than for instantaneous fields. The blockage of the jets appears at the first row of holes. The temperature is cooler within the hole wakes, which is due to

the strong temperature gradients observed during the suction phase.

The wall heat transfer can also be considered through the study of the convective heat transfer coefficient h . Figure 14 compares the numerical results, averaged over five periods, with the mean experimental data, along the symmetry line. There, similar conclusions to what was stated regarding the aerodynamic fields can be drawn: simulations with M1 predict the main tendencies but overestimates the levels. On the contrary, simulations with M2 are close to the experimental results.

Here again, the results are coherent with the other elements previously described: the boundary layer is developing between the inlet and the first row of holes, leading to a decreasing heat transfer coefficient; in the holes area, the transfer increases, due to the enhanced turbulence creating vortices; finally, downstream the holes, the heat transfer coefficient starts to decrease.

CONCLUSION

Synthetic jets present interesting features for heat exchange enhancement. Pprime laboratory developed an experimental set-up to study their impact on heat transfer, in a crossflow, multi-perforation configuration. In the present study, Large Eddy Simulations of this set-up were presented. A user-defined, coarse mesh was used for a first simulation that led to an automatically adapted mesh generation, targeting wall-resolved simulations. Comparisons between the experimental data and the numerical results showed that this second mesh is fine enough to retrieve the correct behaviour of the boundary layer. A simulation run on the refined mesh was used to investigate the boundary layer development. In particular, the axial velocity and wall shear stress were considered. Results showed two distinct flow behaviours, regarding the considered jet mid-period. During the ejection mid-period, the jets trigger unstable shear layers that lead to the formation of vortices, and the level of turbulence increases. The overview of the Q criterion enabled the identification of different flow structures created by the jets during this phase. On the contrary, during the suction mid-period, the flow is sucked within the cavities: the boundary layer is stabilised and a significant rise of the wall shear stress is induced within the hole wakes. These different parameters were then compared to the wall temperature field to better understand the synthetic jets impact on the wall heat transfer. It appears that the vortices created during the ejection bring the cold incoming air nearer to the plate, leading to a thinner boundary layer and lower wall temperatures. During the suction mid-period, the cooling becomes particularly efficient within the hole wakes, because of the boundary layer suction. A new boundary layer restarts at the end of each hole. On the contrary, between the hole lines, the boundary layer is still developing. Thermal gradients are thus high in the transverse direction: temperatures are high between the holes, but low within their wake. This leads to an average temperature field where the synthetic jets lead to global cooling of the perforated plate, marked by the suction mid-period thermal gradients and some of the ejection mid-period structures. Finally in the hole wakes a good comparison with experimental data and numerical simulation is found on the convective heat transfer coefficient, and these results are coherent with the

analysis of the boundary layer development.

ACKNOWLEDGMENT

The authors acknowledge the DGAC OPTIMA (OPTimisation Thermique de l'Intégration des Moteurs d'Avions) project for funding this research and Airbus as a project partner. We also thank Institut Pprime and especially B. Giachetti and M. Fénot for the experimental data. This work was granted access to the HPC resources of CINES/IDRIS under the allocation 2018-A0042A06074 made by GENCI.

NOMENCLATURE

ACRONYMS

ALE Arbitrary Lagrangian Eulerian
CFD Computational Fluid Dynamics
DNS Direct Numerical Simulation
LES Large-Eddy Simulation
LODI Local One Dimensional Inviscid
NSCBC Navier-Stokes Characteristic Boundary Condition
TTGC Two-Step Taylor Galerkin C
rms Root Mean Square

GREEK LETTERS

Φ Non-dimensional value for the metric [-]
 α Parameter for the metric to control the cell dilatation [-]
 $\varepsilon_{min}, \varepsilon_{max}$ Thresholds for the metric [-]
 ϕ Wall heat flux [$W.m^{-2}$]
 ν Kinematic viscosity of air [$m^2.s^{-1}$]

SYMBOLS

A Perforation area [m^2]
 D Perforation diameter [m]
 f Pistons frequency [Hz]
 h Convective heat transfer coefficient [$W.m^{-2}.K^{-1}$]
 K Pistons amplitude [m]
 L_0 Synthetic jet stroke length [m]

- Nu Nusselt number [–]
 Re Reynolds number [–]
 St Strouhal number [–]
 T Period of the pistons motion [s]
 T_w Wall temperature [K]
 t Time [s]
 \vec{U} Velocity [$m.s^{-1}$]
 U_0 Freestream axial velocity [$m.s^{-1}$]
 \bar{W} Average jet vertical velocity along the ejected mid-period [$m.s^{-1}$]
 u, v, w Axial, transverse and vertical velocity components [$m.s^{-1}$]
 x, y, z Axial, transverse and vertical coordinates [m]
 Y^+ Normalized wall distance [–]
 $Z_{pistons}$ Pistons vertical position [m]
 Z_{mean} Pistons mean vertical position [m]

REFERENCES

- [1] Amitay, M. and Glezer, A., 2006. “Aerodynamic flow control using synthetic jet actuators”. In Koumotsakos P., Mezić I. (eds) *Control of Fluid Flow. Lecture Notes in Control and Information Sciences*, **330**. Springer, Berlin, Heidelberg.
- [2] Arik, M. and Sharma, R. and Lustbader, J. and He, X., 2013. “Steady and Unsteady Air Impingement Heat Transfer for Electronics Cooling Applications”. *Journal of Heat Transfer*, **135**(11).
- [3] Trávníček, Z. and Tesař, V., 2003. “Annular synthetic jet used for impinging flow mass-transfer”. *International Journal of Heat and Mass Transfer*, **46**(17), pp. 3291-3297.
- [4] Duchaine, F., 2017. “Sensitivity analysis of heat transfer in a honeycomb acoustic liner to inlet conditions with large eddy simulation”. In ASME Turbo Expo 2017: Turbine Technical Conference and Exposition, no. GT2017-63243. Charlotte, North Carolina, USA, June 2017.
- [5] Holman, R. and Utturkar, Y. and Mittal, R. and Smith, B. L. and Cattafesta, L., 2005. “Formation Criterion for Synthetic Jets”. *AIAA Journal*, **43**(10), pp 2110-2116.
- [6] Smith, B. L. and Swift, G. W., 2001. “Synthetic Jets at Large Reynolds Number and Comparison to Continuous Jets”. In 15th AIAA Computational Fluid Dynamics Conference. Anaheim, CA, USA, June 2001.
- [7] Smith, B. L. and Swift, G. W., 2003. “A comparison between synthetic jets and continuous jets”. *Experiments in Fluids*, **34**(4), pp 467-472.

- [8] Leschziner, M. A. and Lardeau, S., 2011. "Simulation of slot and round synthetic jets in the context of boundary-layer separation control". *Philosophical Transactions of the Royal Society A*, **369**, pp 1495-1512.
- [9] Lardeau, S. and Leschziner, M. A., 2011. "The interaction of round synthetic jets with a turbulent boundary layer separating from a rounded ramp". *Journal of Fluid Mechanics*, **683**, pp 172-211.
- [10] Bocquet, S. and Jouhaud, J.-C. and Deniau, H. and Boussuge, J.-F. and Estève, M. J., 2014. "Wall-Modelled Large-Eddy Simulation of a hot Jet-In-Cross-Flow with turbulent inflow generation". *Computer and Fluids*, **101**, pp 136-154.
- [11] Ruiz, A. M. and Lacaze, G. and Oefelein, J. C., 2015. "Flow topologies and turbulence scales in a jet-in-cross-flow". *Physics of Fluids*, **27** (4).
- [12] Nae, C., 2000. "Unsteady flow control using synthetic jet actuators". in AIAA Fluids 2000 Conference and Exhibit, Denver, CO, USA, June 2000.
- [13] Wen, X. and Tang, H., 2014. "On hairpin vortices induced by circular synthetic jets in laminar and turbulent boundary layers". *Computer and Fluids* **95**, pp 1-18.
- [14] Yang, S. L. and Spedding, G. R., 2013. "Passive separation control by acoustic resonance". *Experiments in Fluids* **47**.
- [15] Bodart, J. and Shelekhov, G. and Scalo, C. and Joly, L., 2017. "Separation delay via hydro-acoustic control of a NACA4412 airfoil in pre-stalled conditions". in 55th AIAA Aerospace Sciences Meeting, Grapevine, Texas, USA, January 2017.
- [16] Zhang, Q. and Bodony, D. J., 2016. "Numerical investigation of a honeycomb liner grazed by laminar and turbulent boundary layers". *Journal of Fluid Mechanics* **792**, pp. 936-980.
- [17] Aillaud, P., 2017. "Simulation aux Grandes Echelles pour le refroidissement d'aubage de turbine haute-pression". PhD thesis, Université de Toulouse, INP Toulouse - Ecole doctorale MEGeP.
- [18] Persoons, T. and Mcguinn, A. and Murray, D. B., 2011. "A general correlation for the stagnation point Nusselt number of an axisymmetric impinging synthetic jet". *International Journal of Heat and Mass Transfer* **54**(17-18), pp. 3900-3908.
- [19] Mcguinn, A. and Farrelly, R. and Persoons, T. and Murray, D. B., 2013. "Flow Regime Characterisation of an Impinging Axisymmetric Synthetic Jet". *Experimental thermal and fluid science* **47**, pp. 241-251.
- [20] Manning, P. and Persoons, T. and Murray, D. B., 2014. "Heat transfer and flow structure evaluation of a synthetic jet emanating from a planar heat sink". *Journal of Physics: Conference Series* **525**.
- [21] Giachetti, B. and Fénot, M. and Couton, D. and Plourde, F., 2018. "Influence of Reynolds number synthetic jet dynamic in crossflow configuration on heat transfer enhancement". *International Journal of Heat and Mass Transfer* **118**, pp 1-13.
- [22] Giachetti, B. and Fénot, M. and Couton, D. and Plourde, F., 2018. "Influence of multi-perforation synthetic jet configuration on heat transfer enhancement". *International Journal of Heat and Mass Transfer* **125**, pp. 262-273.
- [23] P. D. Lax and B. Wendroff, 1960. "Systems of conservation laws". *Commun. Pure Appl. Math.* **13** (2), pp. 217-237.

[24] J. Smagorinsky, 1963. "General circulation experiments with the primitive equations: 1. The basic experiment". *Monthly Weather Review* **91**, pp. 99-164.

[25] Nicoud, F. and Baya Toda, H. and Cabrit, O. and Bose, S. and Lee, J. , 2011. "Using singular values to build a subgrid-scale model for Large Eddy Simulations". *Physics of Fluids* **23** (8).

[26] T. Poinso and S. K. Lele, 1992. "Boundary conditions for direct simulations of compressible viscous flows". *Journal of Computational Physics* **101** (1), pp. 104-129.

[27] Granet, V. and Vermorel, O. and Léonard, T. and Gicquel, L.t and Poinso, T., 2010. "Comparison of Nonreflecting Outlet Boundary Conditions for Compressible Solvers on Unstructured Grids". *AIAA Journal* **48** (10), pp. 2348-2364.

[28] Moureau, V. and Lartigue, G. and Sommerer, Y. and Angelberger, C. and Colin, O. and Poinso, T., 2005. "Numerical methods for unsteady compressible multi-component reacting flows on fixed and moving grids". *Journal of Computational Physics* **202** (2), pp. 710-736.

[29] Daviller, G. and Brebion, M. and Xavier, P. and Staffelbach, G. and Mueller, J.-D. and Poinso, T., 2017. "A mesh adaptation strategy to predict pressure losses in LES of swirled flows". *Flow Turbulence and Combustion* **99** (1), pp. 93-118.

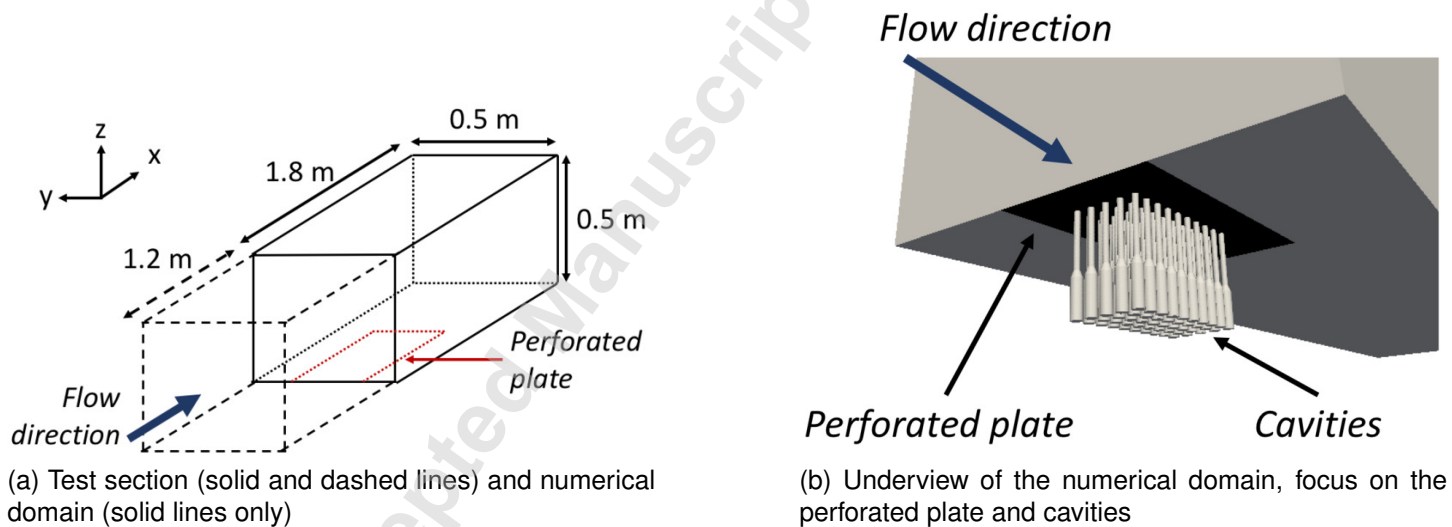


FIGURE 1: Geometry

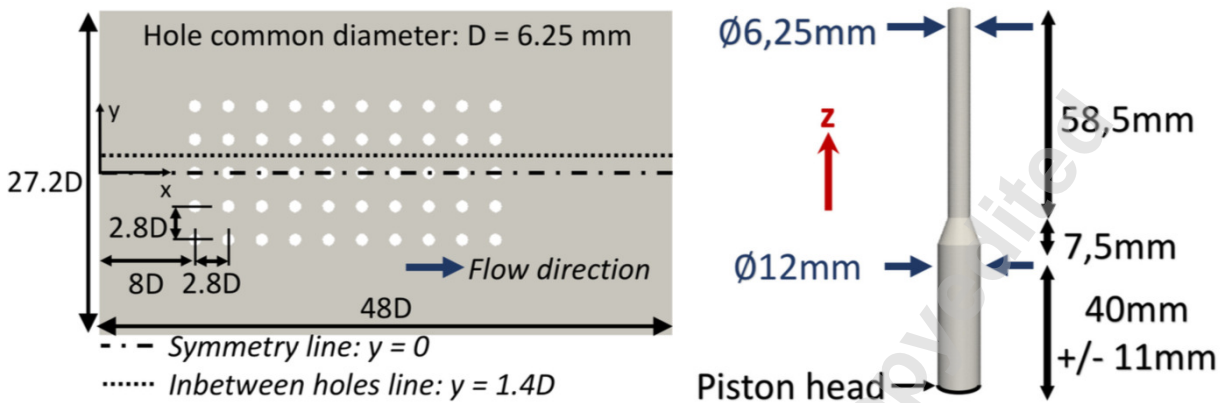


FIGURE 2: Perforated plate, cavities and pistons

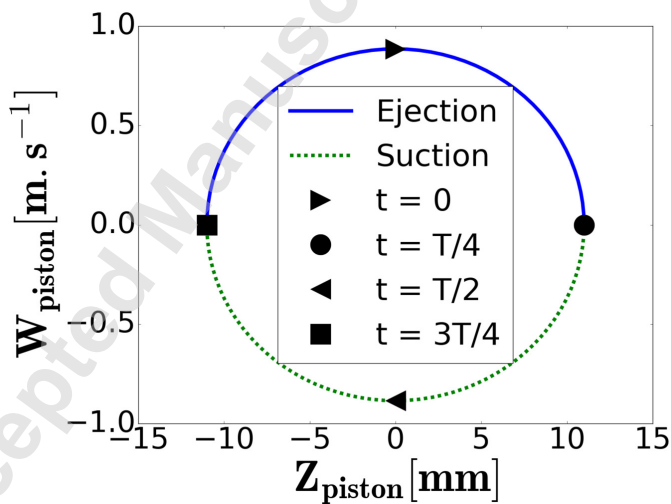


FIGURE 3: Pistons motion along a period T

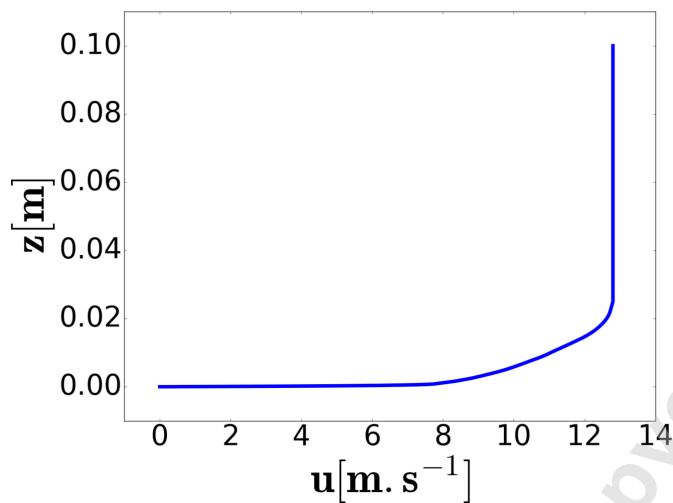


FIGURE 4: Axial velocity profile injected at inlet

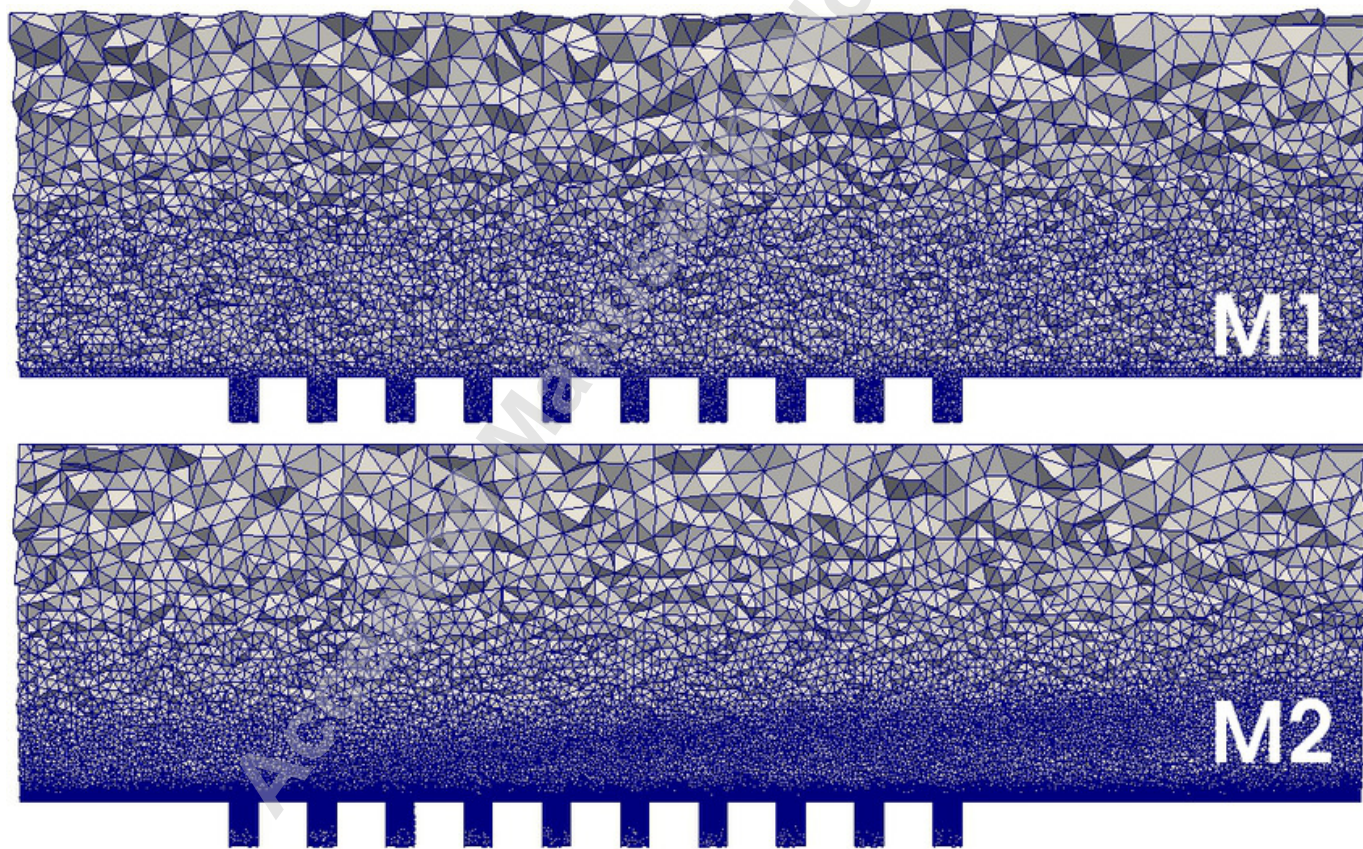


FIGURE 5: Comparison of M1 and M2 on a cut along the symmetry plane of the domain; focus on the perforated plate zone

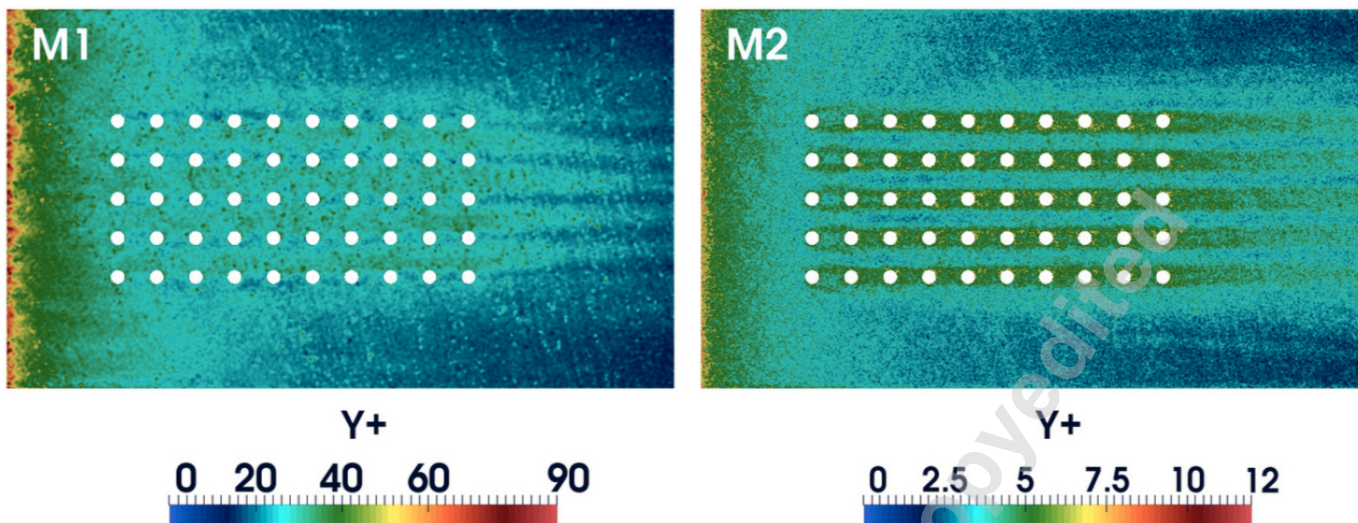


FIGURE 6: Comparison of wall Y^+ fields on the perforated plate, for meshes M1 and M2; fields averaged over five periods

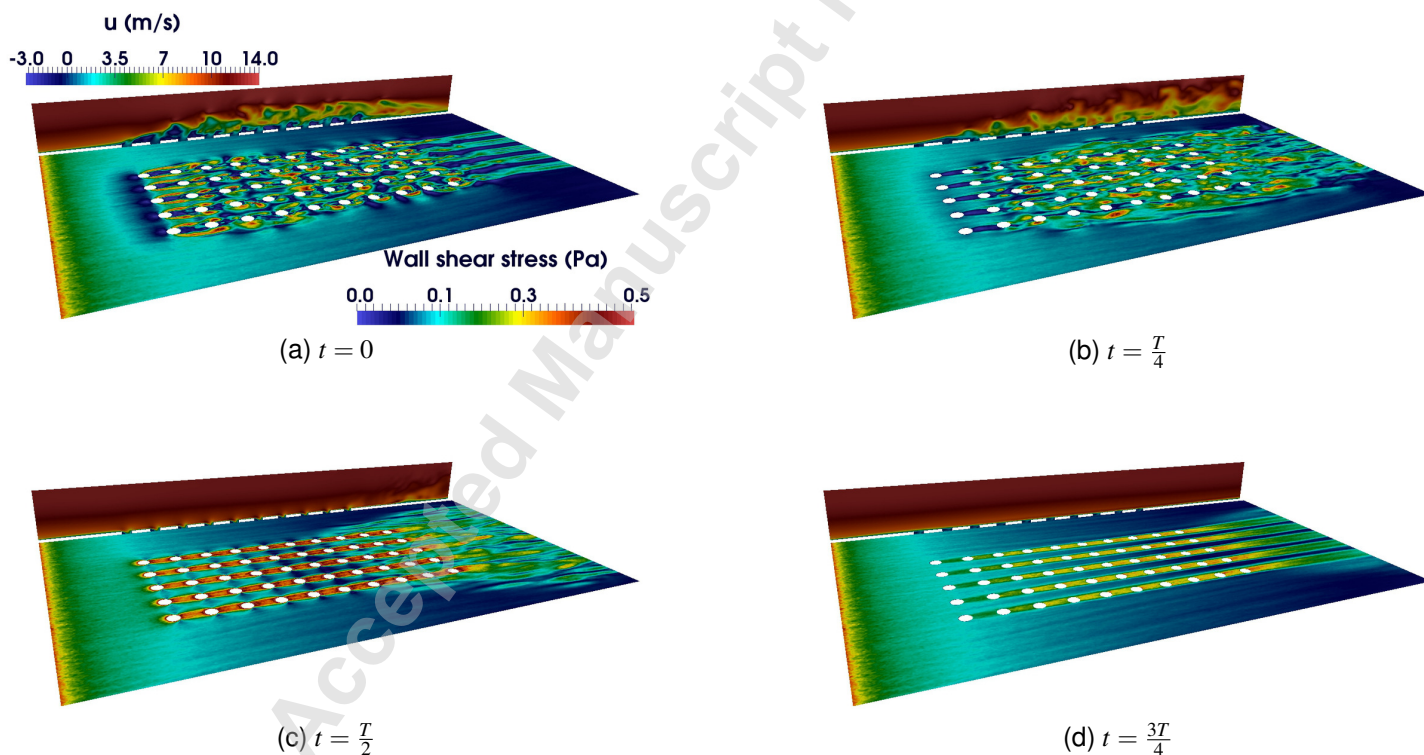


FIGURE 7: Instantaneous axial velocity field in the symmetry plane with wall shear stress along the perforated plate, at different times distributed on a period T , mesh M2

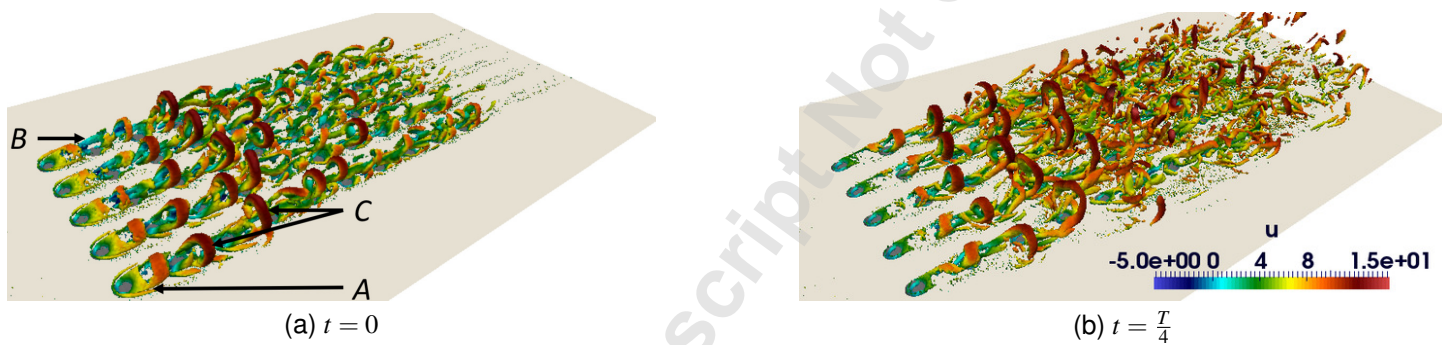
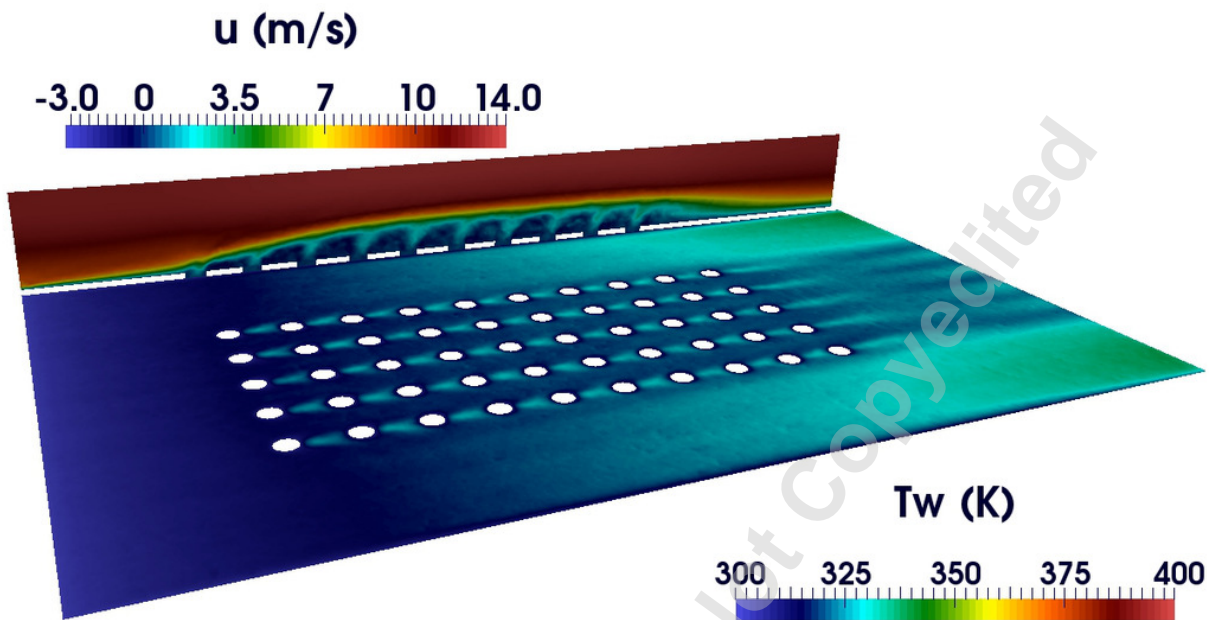
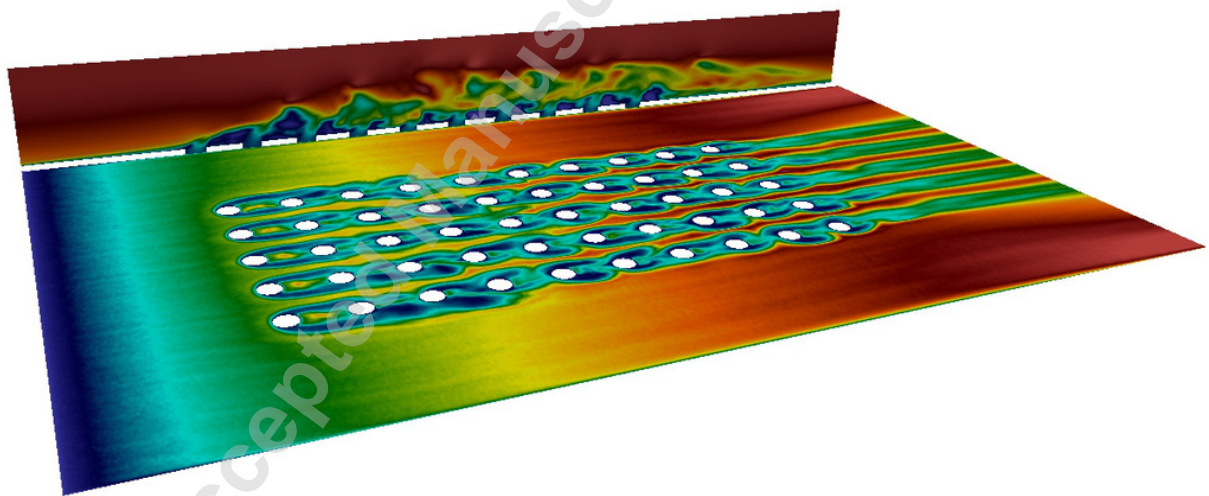


FIGURE 8: Q criterion colored by the axial velocity ($\text{m}\cdot\text{s}^{-1}$), during the ejection mid-period. Simulation run on mesh M2.

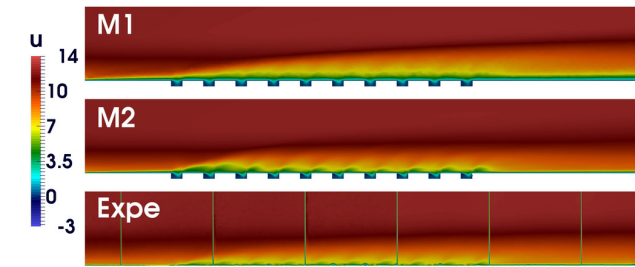


(a) Mesh M1

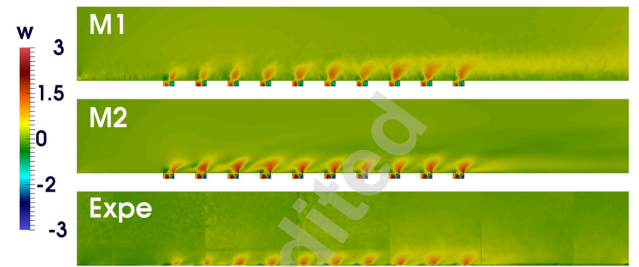


(b) Mesh M2

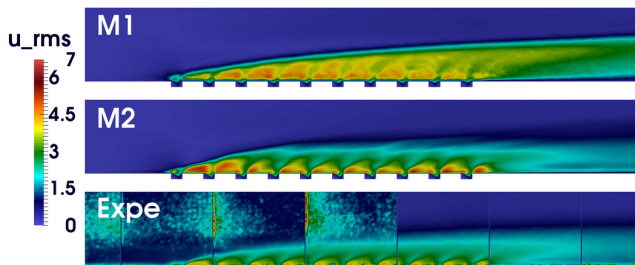
FIGURE 9: Meshes M1 and M2, axial velocity on the symmetry plane and plate temperature instantaneous fields, $t = 0$



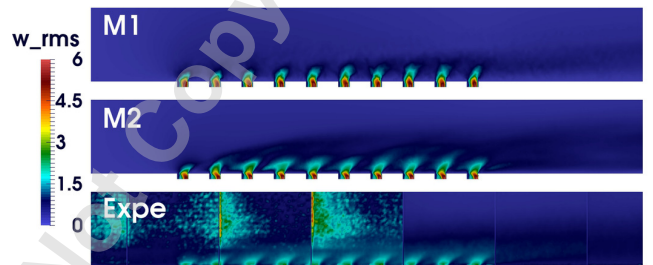
(a) Mean axial velocity ($\text{m}\cdot\text{s}^{-1}$) along symmetry plane



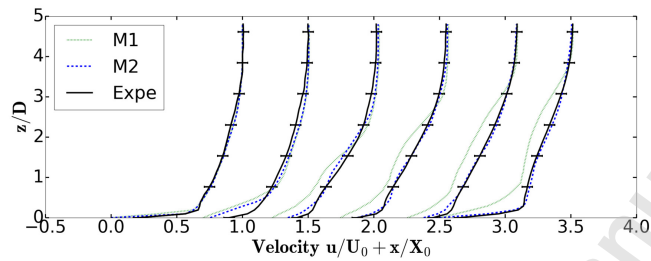
(b) Mean vertical velocity ($\text{m}\cdot\text{s}^{-1}$) along symmetry plane



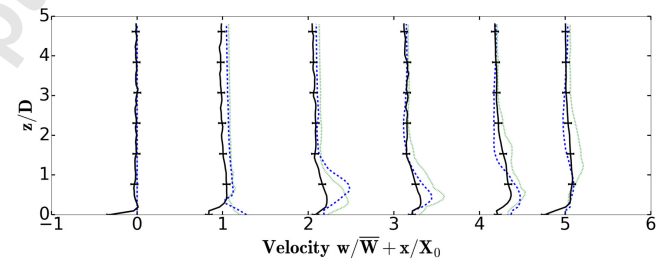
(c) *rms* of axial velocity ($\text{m}\cdot\text{s}^{-1}$) along symmetry plane



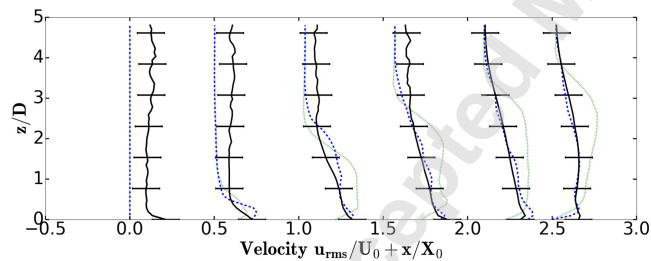
(d) *rms* of vertical velocity ($\text{m}\cdot\text{s}^{-1}$) along symmetry plane



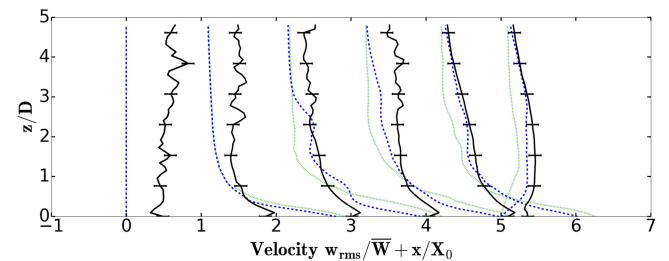
(e) Mean axial velocity profiles



(f) Mean vertical velocity profiles

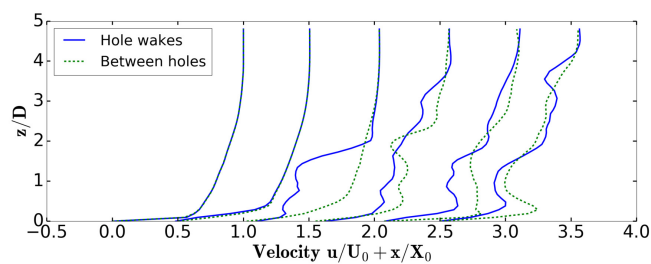


(g) *rms* of axial velocity profiles

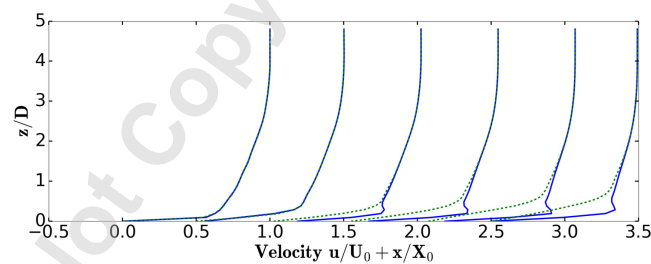


(h) *rms* of vertical velocity profiles

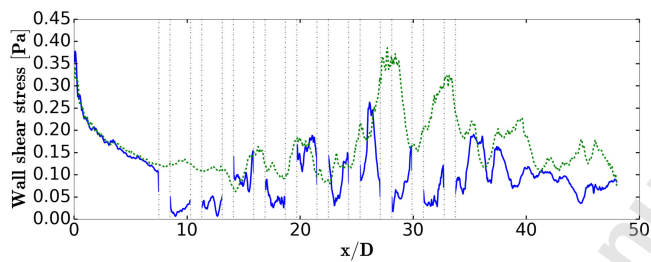
FIGURE 10: Comparison of numerical results on M1, M2 and experimental data. Fields averaged over several periods of the pistons motion



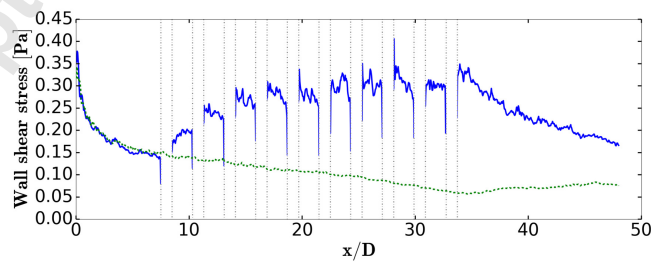
(a) $t = \frac{T}{4}$



(b) $t = \frac{3T}{4}$



(c) $t = \frac{T}{4}$



(d) $t = \frac{T}{4}$

FIGURE 11: Instantaneous axial velocity profiles and wall shear stress along the perforated plate, at different times distributed along a period T . Simulation run on mesh M2.

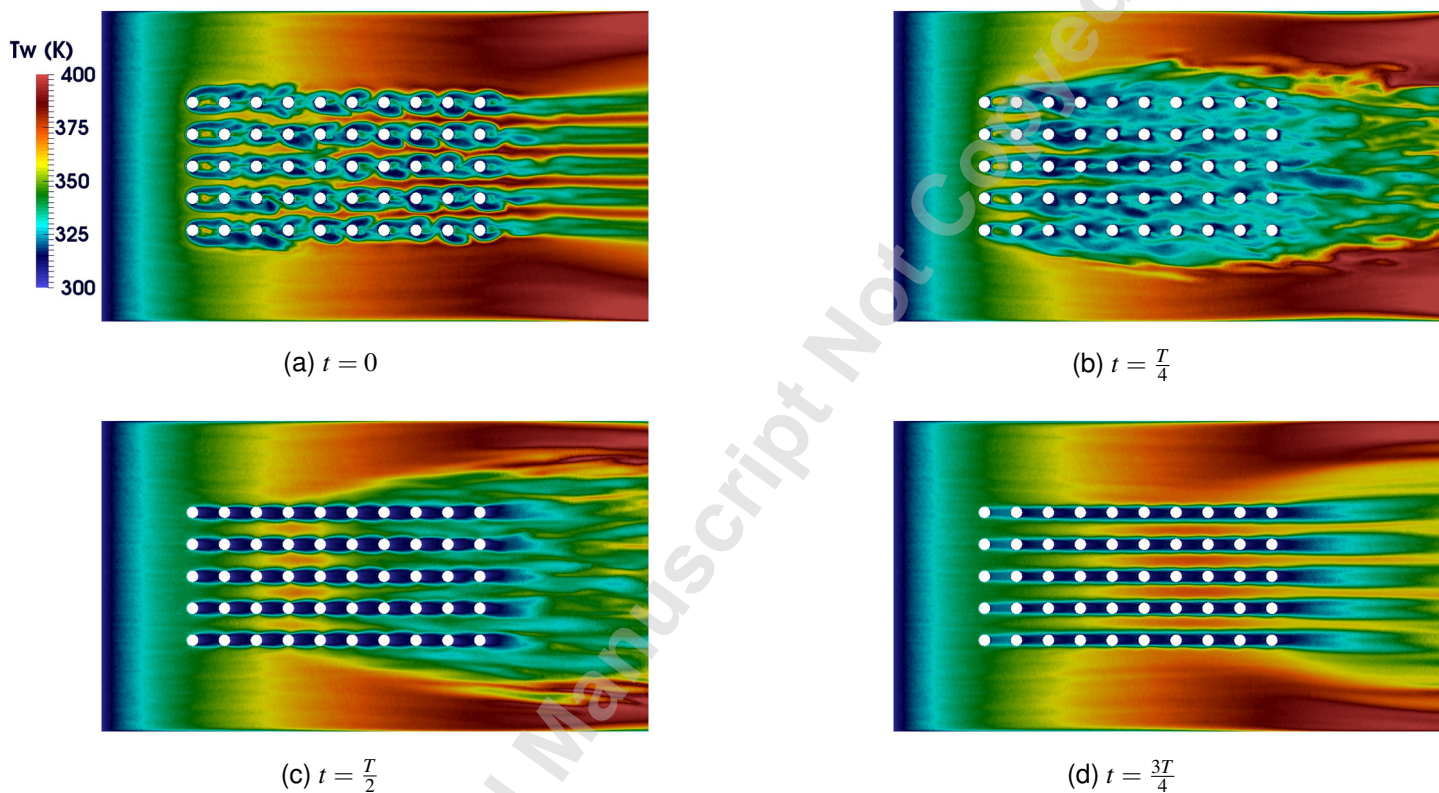


FIGURE 12: Instantaneous plate temperature field along the perforated plate at different times distributed along a period T . Simulation run on mesh M2.

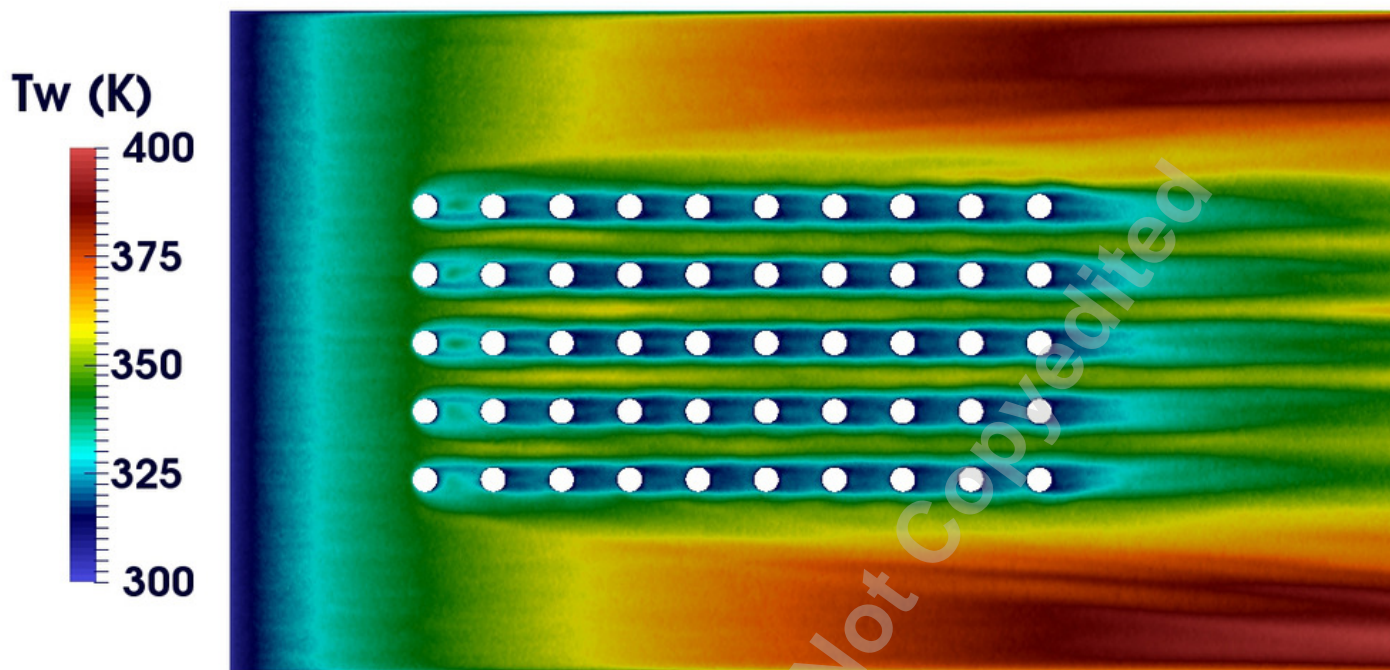


FIGURE 13: Plate temperature field averaged over five periods. Simulation run on mesh M2.

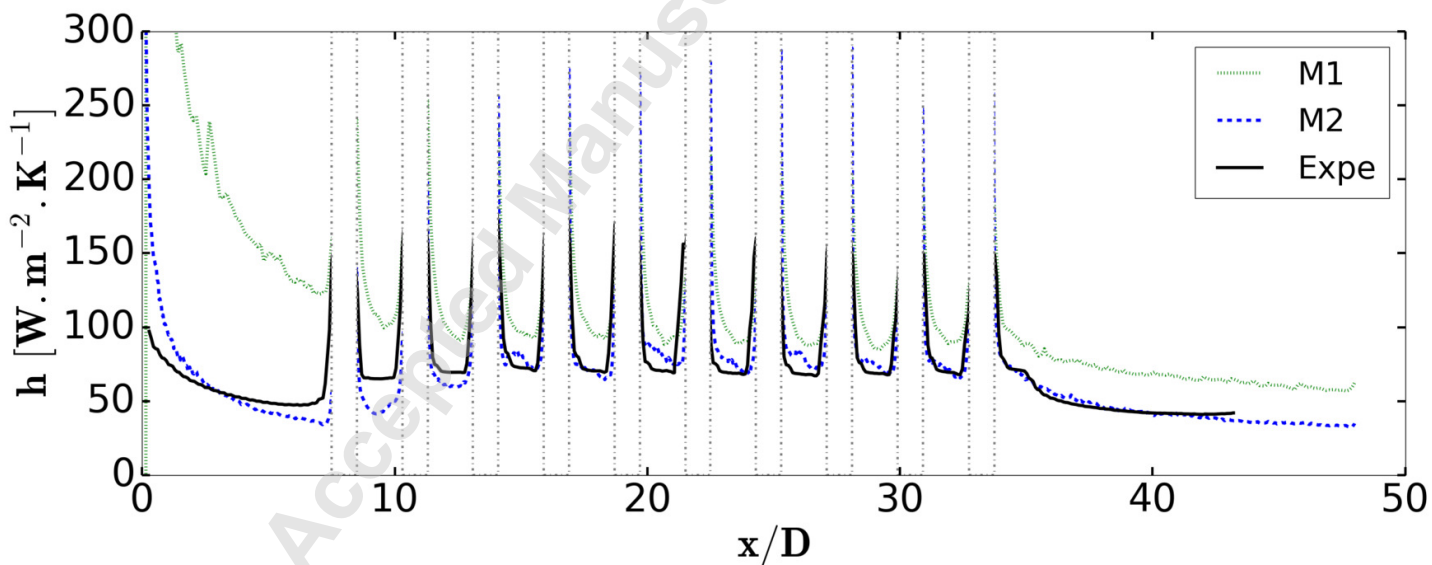


FIGURE 14: Comparison of mean convective heat transfer coefficient, numerical results on M1 and M2 (averaged over five periods) and experimental data, along the symmetry line